Shear-induced platelet margination in a microchannel

Hong Zhao[1] and Eric S. G. Shaqfeh[1,2]
[1]*Department of Mechanical Engineering, Stanford University, Stanford, California, USA*
[2]*Department of Chemical Engineering, Stanford University, Stanford, California, USA*
(Received 28 August 2010; revised manuscript received 26 April 2011; published 30 June 2011)

The lateral migration of platelets in a microchannel is studied numerically where the hydrodynamic interactions between red cells, platelets, and vessel walls are resolved by the Stokes flow boundary integral equations. The simulations provide a clear physical description of the expulsion of the platelets by the velocity fluctuations in the core cellular flow toward the cell-depleted layer near the wall. The lateral migration is shown to be diffusional, and we further demonstrate, in agreement with previous experiments, that the diffusivity scales sublinearly with the shear rate if the relevant capillary number, Ca < 1, as a result of its intrinsic dependence on the deformation of red cells.

DOI: 10.1103/PhysRevE.83.061924 PACS number(s): 87.19.uj, 47.63.−b, 47.15.G−

I. INTRODUCTION

The preferential concentration of platelets near vessel walls is critical for the formation of a hemostatic plug and thrombosis. Note that the predominant nonliquid blood constituent, erythrocytes [or red cells (RBCs)], occupy 36%–53% of the blood volume [1]. The number density of platelets is about 1/10 of RBCs, and their size (2–4 μm in diameter) is significantly smaller than that of RBCs (about 8 μm diameter). Hence the motion of platelets, in both axial and lateral directions, is heavily influenced by the distribution and kinematics of red cells. Known as the famous Fahraeus-Lindquist effect [2], RBCs migrate toward the center of the vessel, leaving a cell-free layer near the wall where the platelets tend to concentrate.

The near-wall concentration of platelets and similar-sized particles, as well as the necessary existence of RBCs for the margination of platelets, has been confirmed in experiments [3,4], though a detailed mechanism is still unavailable. From their platelet adhesion experiments, Aarts *et al.* [5] fit the effective platelet diffusivity to a power law with the wall shear rate, and the exponent is found to depend strongly on the hematocrit. The effective wall normal diffusivity of platelet migration is several orders of magnitude higher than their intrinsic Brownian diffusivity and is considered to be a shear-induced diffusivity due to the hydrodynamic interactions between the platelets and RBCs [3,4]. It is well known that in a rigid particle flow, the particle-particle collisions cause lateral movements; the frequency and intensity of these collisions determine the effective diffusivity of particles, which scales linearly with the flow shear rate [6–8]. In blood flow, because of the much lower number density of platelets as compared to that of the red cells, the shear-induced diffusion of platelets must be dominated by the hydrodynamic interaction between the platelets and red cells. The situation is complicated by the deformability of RBCs, which can be quantified by a capillary number $\mathrm{Ca} = \mu^* \dot{\gamma}^* a^* / E_S^*$, where $\mu^* = 1.2$ mPa $\cdot$ s is the viscosity of blood plasma, $\dot{\gamma}^*$ is a characteristic flow shear rate, $a = 2.82$ μm* is the equivalent radius of a typical human erythrocyte based on its volume, and $E_S^* = 6.8$ μN/m is the shear modulus of a normal RBC membrane [9]. As a result, the platelet diffusivity, when nondimensionalized by $\dot{\gamma}^* a^{*2}$, must depend on Ca, and this dependence is manifest in a nonlinear dependence of the (dimensional) platelet diffusivity on the flow shear rate as observed in experiments [5].

Because of the dominant RBC volume fraction and their larger size, the existence of platelets apparently does not alter the overall flow characteristics in any significant way. Moreover, the hydrodynamic interaction between the RBCs and platelets is expected to be dominated by the former, and the much smaller platelets mainly sample the velocity fluctuations due to the interactions between red cells. These ideas are examined in our present numerical simulation of a pressure-driven blood flow between two flat plates, where the hydrodynamic interactions between RBCs, platelets, and walls are solved fully coupled by a Stokes flow boundary integral equation method. Focusing on the physical mechanism of platelet margination, we investigate the cellular flow's velocity fluctuations, the velocity autocorrelation, and the diffusive spreading of passive non-Brownian tracers as well as platelets, with particular emphasis on their dependence on the flow capillary number.

II. NUMERICAL METHOD

Though the whole blood behaves as a non-Newtonian complex fluid [10], the fluid phase of the blood is essentially Newtonian. In small vessels, the flow is Stokesian due to the nearly zero Reynolds number and can thus be calculated using the boundary integral method [11]. Besides its superior accuracy, the boundary integral method is particularly useful in this context since it obviates the need to mesh the three-dimensional extracellular space, which has a very complex geometry and is continuously deforming. Most of the details of the formulation and numerical scheme used in the present study have been discussed previously [12]. The RBC membrane is modeled as a two-dimensional neo-Hookean material with bending stiffness [13–16], and the surfaces are discretized into piecewise linear triangular mesh elements. The residual force due to deformation is directly calculated by the virtual work principle as the first variation of the elastic and bending energy. Because platelets are much stiffer than RBCs, they are modeled as rigid discoids [17]. We assume that the platelets are not activated and thus neglect their complex surface features [17]. These platelets are free of external forces

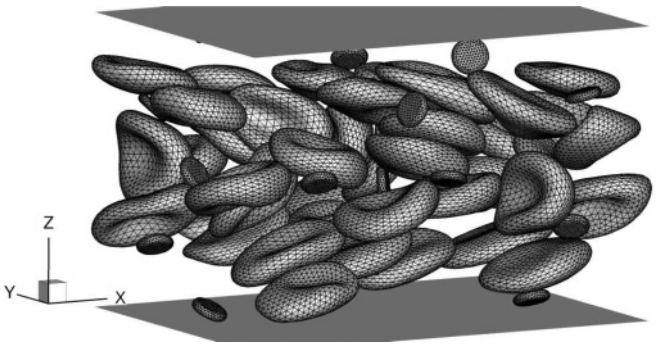

FIG. 1. Boundary integral equation simulation of red cells and platelets in a channel flow.

and torques, and their rigid body motion is solved by a deflated double-layer formulation [11].

The RBC surface velocity, the wall friction force, and the double-layer density on the platelet surfaces are solved fully coupled after the discretization of the boundary integral equations, where the left-hand side matrix can be decomposed into 3×3 submatrices that represent the hydrodynamic interactions between the three subsystems. The resulting linear equation is solved by a matrix-free GMRES solver without explicitly forming the dense matrix. The matrix-vector multiplication needed by the iterative solution is formed implicitly via directly computing the surface integrals at collocation points and is accelerated by the smooth particle mesh Ewald sum method with $O(N \log N)$ computational cost, where N is the total number of surface mesh points [12,18].

As shown in Fig. 1, the channel flow is between two infinite flat plates with the wall normal direction along the z axis and is periodic in the x and y directions. A background velocity $\langle \mathbf{u} \rangle$ is applied in the x direction to drive the flow, and it is easy to show that $\langle \mathbf{u} \rangle$ is the volume-averaged velocity in the computation domain. This is equivalent to applying a mean pressure gradient $\langle \partial p/\partial x \rangle$. The relation between $\langle \mathbf{u} \rangle$ and $\langle \partial p/\partial x \rangle$ in principle depends on the instantaneous flow configuration; however, the fluctuations in $\langle \partial p/\partial x \rangle$ at constant $\langle \mathbf{u} \rangle$ always remain less than 1% in a stationary state.

All quantities are nondimensionalized by the RBC radius a^*, the plasma viscosity μ^*, and a characteristic shear rate $\dot{\gamma}^* = 6\langle u \rangle^*/H^*$ that is the wall shear rate of the Poiseuille flow in the same channel of height H^*. Hence a unit capillary number corresponds to a wall shear rate of approximate 2000 s^{-1}. The membrane's dilatational modulus E_D^* is chosen as a penalty parameter so that $\mu^* \dot{\gamma}^* a^*/E_D^* = 10^{-2}$, and the change in the local RBC surface area (defined as $\Delta A/A$, where A is the area of an RBC surface mesh element) is less than 0.5% on average. Moreover, the local area change per element is less than 3% for 90% of all elements over the entire range of Ca investigated. The nondimensional membrane bending stiffness is $E_B = E_B^*/(E_S^* a^{*2}) = 3.3 \times 10^{-3}$.

The computational domain has a length $L = 16$ in the flow direction and a height $H = 12$. The spanwise size is 9, which is more than three times the RBC diameter, thus allowing fully three-dimensional flow development. Although the normal range of human body hematocrit is 40%–50%, the local hematocrit drops significantly in small vessels and is only about 40% of the body average at 30 μm vessel diameter [19,20]. Hence the mean hematocrit $\langle H_t \rangle$ in this study is chosen to be 0.2. At Ca $= O(1)$ and with an initial random disposition of undeformed red cells, more than 50 flow-through times $(L/\langle u \rangle)$ are typically necessary to establish a stationary cellular distribution. This corresponds to a relaxation time of about 400, which is of the same order as the relaxation time scale $(H/a)^3 a/\langle u \rangle = 864$ for rigid particulate flows [8].

III. RESULTS

The snapshots of the full system simulations at Ca $= 0.25$ and 2 are shown in Fig. 2. The cell-depleted Fahraeus-Lindquist zone is clearly visible, and the RBCs immediately next to the cell-free layer are aligned with flow. The width of the cell-depleted layer is implicitly determined by the balance between the wall lift velocity of the cells and the intercell interactions. At Ca $= 0.25$, the cells exhibit strong resemblance to the biconcave shapes in the stress-free state, especially near the center line where the local shear rate is the lowest. At Ca $= 2$, cells close to the wall are significantly elongated and are more uniformly aligned with the flow; cells near the center line have slipper-like shapes similar to those in a capillary flow [21]. Because the cellular shapes change with the capillary number, the flow characteristics must also depend on Ca, which ultimately determines the Ca dependence of the particle migration in the flow.

Figure 3 shows the dimensionless mean axial velocity profile as well as the root mean square (RMS) of the wall normal velocity fluctuations $\sqrt{\langle w^2 \rangle}$, with both normalized by $\dot{\gamma}_w a$, where $\dot{\gamma}_w$ is the wall shear rate and $a \equiv 1$ by nondimensionalization. Inside the cell-depleted layer, the mean velocity profiles collapse to the Poiseuille profile but become blunt inside the cell-laden region. The flow is shear thinning, as the deviation of the center-line velocity from that of the Poiseuille flow is reduced with increasing Ca. With respect to the reference shear rate $\dot{\gamma}^* = 6\langle u^* \rangle/H^*$, the wall shear rate $\dot{\gamma}_w$ decreases from 1.22 at Ca $= 0.25$, to 1.13 at Ca $= 2.0$, meaning a reduction in the wall friction force and equivalently a reduction in the apparent blood viscosity.

In the cell-depleted layer, the normal velocity fluctuations are zero at the wall because of the no-slip boundary condition. The fluctuations increase monotonically as the core cellular region is approached and are maximal at $z \approx 3$, which, roughly speaking, is the dividing plane between the first and second layers of RBCs away from the Fahraeus-Lindquist zone. This is also where the maximal local shear rate occurs inside the cell-laden region. The value of $\sqrt{\langle w^2 \rangle}$ then decreases further as the channel center line is approached but remains nonzero

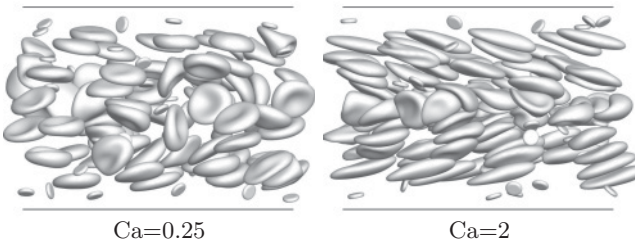

FIG. 2. The snapshots of the system at Ca $= 0.25$ and 2.

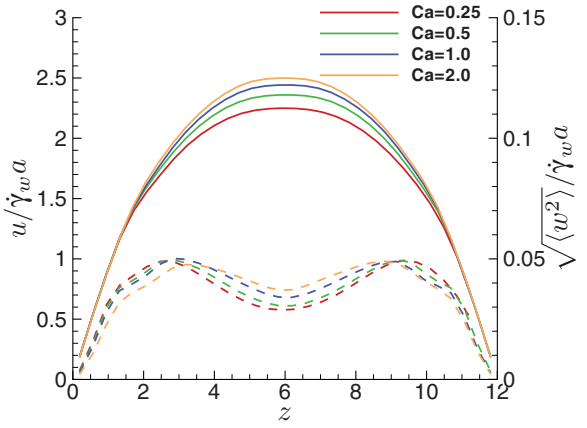

FIG. 3. (Color online) The mean axial velocity (solid line) and the RMS of wall normal velocity fluctuation (dashed lines), both normalized by the wall velocity scale $\dot{\gamma}_w a$.

even at $z = H/2$, where the local mean shear rate is zero. This nonlocal effect certainly results from the fact that the RBC radius is comparable to the channel height and is consistent with previous findings of the nonzero center-line suspension temperature in a channel flow of a suspension of rigid spheres [8].

The wall normal velocity fluctuations are fully characterized by the autocorrelation of Lagrangian tracers, which are placed randomly in the extracellular region and then passively convected by the flow. The channel is divided equally into 12 intervals in the z direction; for spatial binning, the correlation $w(t)w(t + \Delta t)$ is assigned to the z interval within which the tracer at time t lies. The normalized autocorrelation curves at $z = 1$ (inside the cell-free layer) and at $z = 6$ (at the center line) are shown in Fig. 4. At $z = 1$, the curves of different Ca overlap well when t is scaled by the wall shear rate $\dot{\gamma}_w$. At $z = 6$, we have found that these curves collapse reasonably well, at least for the initial decay near $t = 0$, if the correlation is plotted against $\dot{\gamma}_{\text{core}} t$ where $\dot{\gamma}_{\text{core}} = (u|_{z=6} - u|_{z=3})/3$, which is an empirically defined effective shear rate in the core flow region.

The correlation curve in the core flow region is oscillatory, indicating multiple encounters of a tracer particle with RBCs as it is convected by the flow. The autocorrelation diminishes faster with time at low Ca number, which is qualitatively attributed to the more disordered RBC alignment and spatial distribution (see Fig. 2). At the center line, the negative autocorrelation at $\dot{\gamma}_{\text{core}} t \approx 2$ becomes more significant as Ca increases from 0.25 to 1. The relaxation time τ, which is the integral of autocorrelation, is thus significantly reduced with increasing Ca, as shown in Fig. 4. Since the diffusion coefficient is proportional to $\dot{\gamma}_w^2 \tau$ or alternatively $\dot{\gamma}_{\text{core}}^2 \tau$, and because τ decreases faster than any inverse shear rate, the nondimensional diffusivity decreases with increasing Ca. This is equivalent to saying that the dimensional diffusivity scales sublinearly with any characteristic shear rate in the system at Ca < 1. This can be contrasted to the shear-induced diffusivity in athermal sphere suspensions [8,22], which must be linear with the flow shear rate on dimensional grounds. The reduction in the relaxation time with increasing Ca stops at Ca > 1, and Fig. 4 shows that there is little difference between the τ

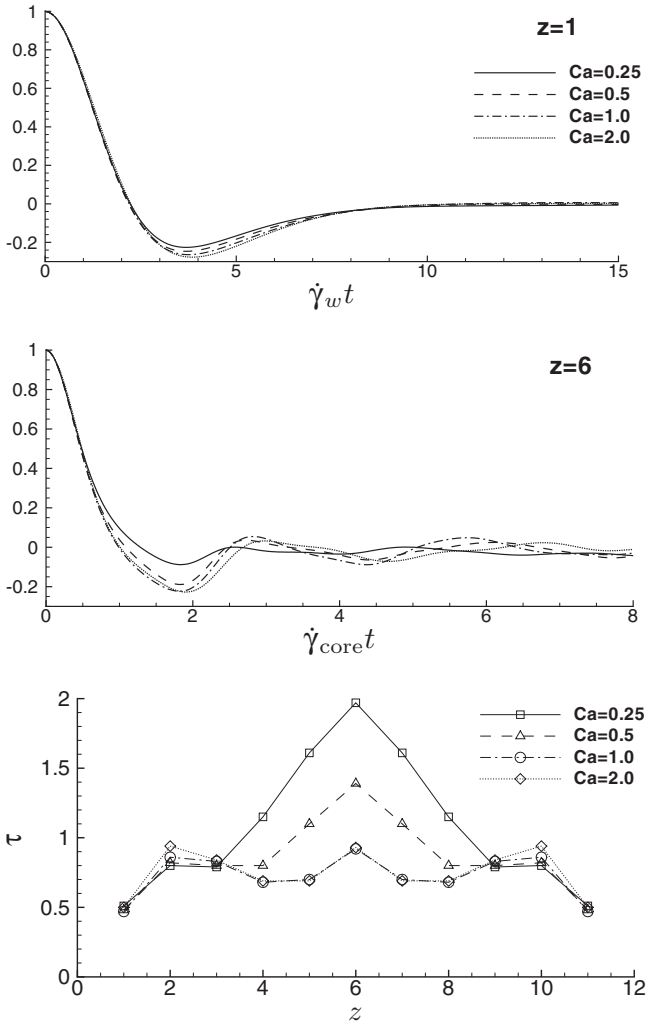

FIG. 4. Top and middle: The normal velocity autocorrelation of Lagrangian tracers at $z = 1$ and 6. Bottom: The profiles of tracer points' relaxation time.

profiles between Ca $= 1$ and 2. Because of the membrane's incompressibility, the elongation of RBCs is saturated at high enough shear rate. Hence τ, which is modulated by the RBC deformation, also becomes insensitive to the capillary number.

Because of their small size, the introduction of platelets does not change the mean axial velocity or the velocity fluctuations significantly. Furthermore, the velocities of the platelets themselves follow those of tracers. Figure 5 compares the x velocities and RMS z velocities for tracers and platelets at Ca $= 1$. There is no visual difference between the two regarding their mean axial velocities, and their RMS z velocities differ by less than 10%.

Figure 6 shows the mean-square displacement $\langle \Delta z^2 \rangle = \langle [z(t) - z(0)]^2 \rangle$ of tracers and platelets, where the slope $d\langle \Delta z^2 \rangle(\tau)/d\tau$ is twice the normal diffusivity $D_\perp$. The curves for platelets (plotted in dashed lines) are qualitatively similar to those of tracers. During their spreading, tracer points sample velocity fluctuations at different z planes; it follows that the spread width is comparable to the channel height when the asymptotic linear spreading rate is established. As a result, we have found only minor variations of spreading speed in the

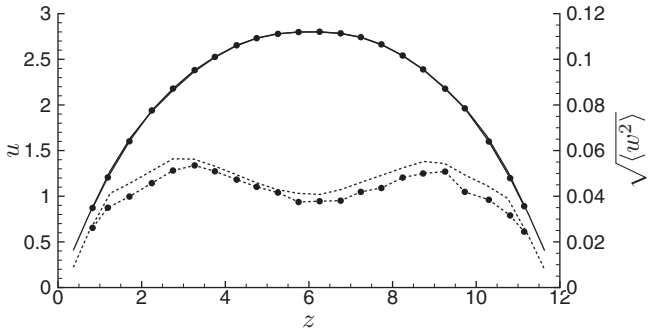

FIG. 5. The mean axial velocities (solid lines) and RMS normal velocities (dashed lines) of tracers and platelets. The lines with symbols denote quantities for platelets.

core flow region. Only $\langle \Delta z^2 \rangle$ averaged over the whole core region is plotted for clear visualization. The $D_\perp$ of tracers decreases by 30% as Ca increases from 0.25 to 1 but levels off at higher Ca. The trend is consistent with the Ca dependence of the relaxation time. The diffusivity of platelets is slightly higher than that of the tracer points, but the Ca dependence remains the same.

Figure 7 shows the platelet trajectories in the z direction. The trajectories of those platelets that finally migrate into the cell-free layer are plotted in blue. The margination appears irreversible: Once the platelets are expelled into the cell-depleted layer, the very small velocity fluctuations make it difficult for the platelets to reenter the core region. The platelet number density profile at $t = 4600$ is shown, where the channel is divided into 24 slices in the z direction. Compared with the density profile at an earlier time $t = 200$, more than half of the platelets have moved to the cell-free layer and are trapped there. We note that the slightly asymmetric concentration profile is caused by the bias in the initial platelet distribution that is difficult to control precisely when they are randomly placed near the center line at $t = 0$.

The time evolution of the RMS distance of platelets from the center line is shown in Fig. 8. The time is scaled by the mean

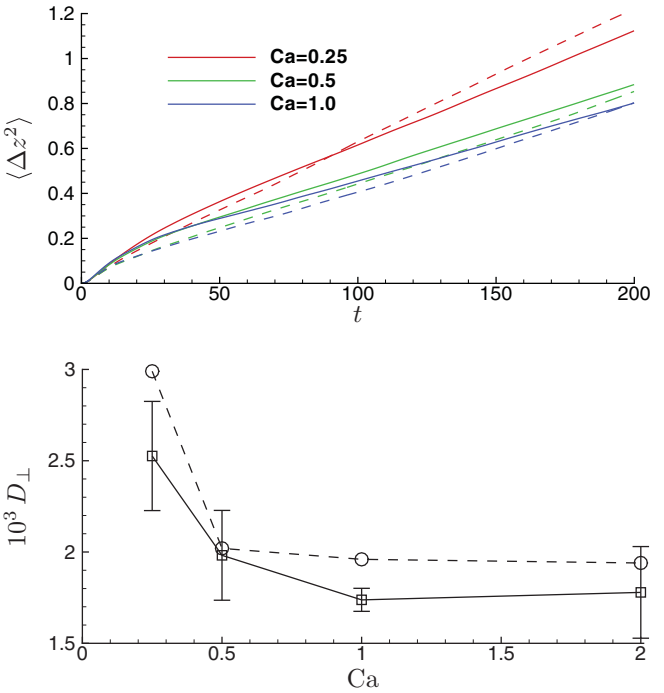

FIG. 6. (Color online) Top: Mean-square displacement in the wall normal direction of tracers (solid lines) and platelets (dashed lines). The statistics is taken for $3 < z < 9$ to exclude the cell-depleted zone. Bottom: The nondimensional diffusivity of tracers (solid line) and platelets (dashed lines).

velocity, and the figure indicates that the speed of the lateral spreading is $O(10^{-3})$ of the convection velocity. Therefore, a platelet will on average travel $O(10)$ mm in the streamwise direction when it migrates from the center line to the wall. This convection length is 20 times that of the average blood vessel branch (about 500 μm) of 34 μm diameter [23]. Therefore, the vessel branches will play a role in determining the equilibrium platelet concentration profile in the microvascular network.

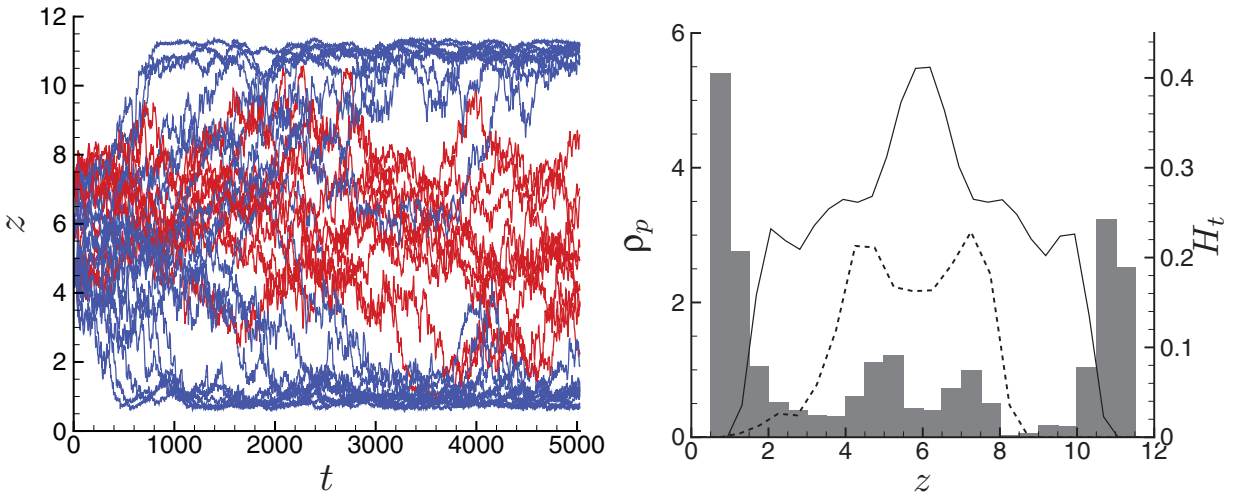

FIG. 7. (Color online) Left: Platelet trajectories in the wall normal direction. Right: The bar chart is the platelet density profile at $t = 4600$; for comparison the dashed line is the density profile at an earlier time $t = 200$, and the solid line is the RBC hematocrit profile. Ca = 1.0 and $\langle H_t \rangle = 0.2$.

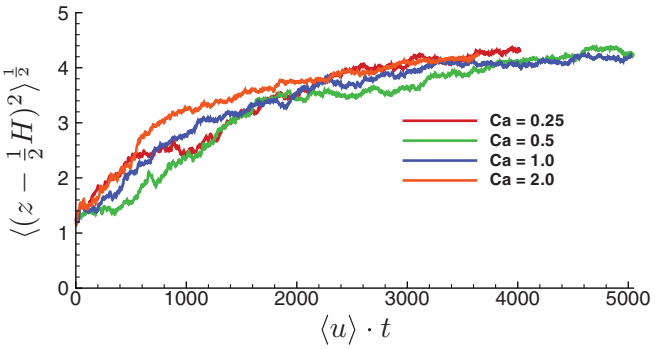

FIG. 8. (Color online) The RMS distance between platelets and channel center line.

IV. DISCUSSION AND CONCLUSION

The incompressibility of an RBC's membrane sets an upper limit to its elongation. With the membrane constitutive model used in this study, the shape elongation saturates when Ca exceeds 1. This gives a qualitative explanation of why $D_\perp$ of tracers and platelets reduces significantly when Ca increases from 0.25 to 1, but almost remains constant with further increase in Ca. The wall shear rate in a vessel of 34 μm diameter is between 2500 s^{-1} (for venules) and 5000 s^{-1} (for arterioles). Thus, the Ca number is greater than 1, and we predict that the (dimensional) platelet diffusivity under such physiological flow conditions should scale linearly with the shear rate because the RBC deformation is saturated.

Experimentally, the diffusivity of platelets in blood has been determined by measuring the adherence rate of platelets to the subendothelial wall of a perfusion chamber. The diffusivity is obtained by fitting the adhesion rate with the theoretical predictions using a transport model of the boundary-layer type [5,24]. The values of diffusivities obtained this way are usually associated with large uncertainties. Turitto and Baumgartner reported $D^* = 2.0 \times 10^{-7}\text{cm}^2/\text{s}$ at $\dot{\gamma}_w = 208\ s^{-1}$, and $D^* = 3.4 \times 10^{-7}\text{cm}^2/\text{s}$ at $\dot{\gamma}_w = 832\ s^{-1}$ for an unknown hematocrit. These translate to the nondimensional $D = 1.2 \times 10^{-2}$ at Ca $= 0.1$, and $D = 5.1 \times 10^{-3}$ at Ca $= 0.4$, which are of the same order of magnitude as our calculation ($D \approx 2 \times 10^{-3}$ at Ca $= 0.25$ for both platelets and tracers). Aarts *et al.*, however, obtained much lower platelet diffusivities from similar perfusion chamber experiments and the same data-fitting procedure [5]. Using their empirical power law of $D^* \propto \dot{\gamma}_w^{*\,0.54\pm0.03}$ at $0.1 \leqslant \text{Ca} \leqslant 0.6$ and $H_t = 20\%$, the nondimensional diffusivity is $D = 1.2 \times 10^{-3}$ at Ca $= 0.1$ and is 6.2×10^{-4} at Ca $= 0.4$, which is about one-third of our numerical result. We note that these experimental results are for the diffusion in bulk shear flows, which are fundamentally different from the microchannel flow environment considered here.

Saadatmand *et al.* very recently measured the dispersion of microbeads of 1 μm diameter in a cylindrical tube of 50 μm diameter, with the hematocrit between 10% and 20% [25]. The geometry is thus quite similar to that in our simulation, while the Ca in the experiment is less than 0.1. The diffusivity of the beads is determined from the linear temporal growth rate of their mean-square displacement in the radial direction. The shear-induced diffusivity of the beads is reported to scale linearly with the wall shear rate; thus the nondimensional $D = 3.6 \times 10^{-3}$ is independent of Ca, which is, however, close to $D = 3.0 \times 10^{-3}$ of platelets at the lowest Ca $= 0.25$ in our simulation.

In summary, we have investigated the margination of platelets in a microchannel by direct numerical simulations that fully resolve the hydrodynamic interactions in the system. It is demonstrated that it is the wall normal velocity fluctuations in the core flow region that expel the platelets toward the wall. The migration is a shear-induced diffusional process where the effective diffusivity, as modulated by the deformation of the red cells, decreases with increasing capillary number but becomes largely independent of Ca for Ca > 1. In the future, the effect of red cell deformability on the diffusivity of particles as well as the RBCs' self-diffusivity warrants more systematic study.

ACKNOWLEDGMENTS

We thank the US Army High Performance Computing Research Center (AHPCRC) for supporting this work. A large portion of the computer simulation was performed on the Stanford University's Certainty computer cluster, which is funded by the American Recovery and Reinvestment Act of 2009 (ARRC).

[1] A. Kratz, M. Ferraro, P. M. Sluss, and K. B. Lewandrowski, N. Engl. J. Med. **351**, 1548 (2004).
[2] R. Fahraeus and T. Lindqvist, Am. J. Physiol. **96**, 562 (1931).
[3] A. W. Tilles and E. C. Eckstein, Microvasc. Res. **33**, 211 (1987).
[4] C. Yeh and E. C. Eckstein, Biophs. J. **66**, 1706 (1994).
[5] P. A. Aarts, P. Steenduk, J. J. Sixma, and R. M. Heethaar, J. Biomech. **19**, 799 (1986).
[6] E. C. Eckstein, D. G. Bailey, and A. H. Shapiro, J. Fluid Mech. **79**, 191 (1977).
[7] D. Leighton and A. Acrivos, J. Fluid Mech. **181**, 415 (1987).
[8] P. R. Nott and J. F. Brady, J. Fluid Mech. **275**, 157 (1994).
[9] J. P. Mills, L. Qie, M. Dao, C. T. Lim, and S. Suresh, MCB **1**, 169 (2004).
[10] S. Chien, S. Usami, H. M. Taylor, J. L. Lundberg, and M. I. Gregersen, J. Appl. Physiol. **21**, 81 (1966).
[11] C. Pozrikidis, *Boundary Integral and Singularity Methods for Linearized Viscous Flow* (Cambridge University Press, Cambridge, UK, 1992).
[12] H. Zhao, A. H. G. Isfahani, L. Olson, and J. B. Freund, J. Comput. Phys. **229**, 3726 (2010).
[13] C. Pozrikidis, Ann. Biomed. Eng. **31**, 1194 (2003).
[14] C. Pozrikidis, Phys. Fluids **17**, 031503 (2005).

[15] J. Li, M. Dao, C. T. Lim, and S. Suresh, Biophs. J. **88**, 3707 (2005).
[16] M. Dao, J. Li, and S. Suresh, Mater. Sci. Eng., C **26**, 1232 (2006).
[17] A. Michelson, *Platelets*, 2nd ed. (Academic Press, New York, 2006).
[18] D. Saintillan, E. Darve, and E. S. G. Shaqfeh, Phys. Fluids **17**, 033301 (2005).
[19] H. H. Lipowsky, S. Kovalcheck, and B. W. Zweifach, Circ. Res. **43**, 738 (1978).
[20] H. H. Lipowsky, S. Usami, and S. Chien, Microvasc. Res. **19**, 297 (1980).
[21] H. Noguchi and G. Gompper, Proc. Natl. Acad. Sci. USA **102**, 14159 (2005).
[22] T. Ishikawa and T. Yamaguchi, Phys. Rev. E **77**, 041402 (2008).
[23] D. Lapi, P. L. Marchiafava, and A. Colantuoni, Vasc. Res. **45**, 69 (2008).
[24] V. T. Turitto and H. R. Baumgartner, Trans. Am. Soc. Artif. Intern. Organs **21**, 593 (1975).
[25] M. Saadatmand, T. Ishikawa, N. Matsuki, M. J. Abdekhodaie, Y. Imai, H. Ueno, and T. Yamaguchi, J. Biomech. **44**, 170 (2011).